metals

MDPI

Article

Image Processing Procedure to Evaluate Inclusion Dissolution in a Slag Observed by High-Temperature Confocal Scanning Laser Microscopy

Shashank Ramesh Babu *, Nikolaus Preisser and Susanne Katharina Michelic

Christian Doppler Laboratory for Inclusion Metallurgy in Advanced Steelmaking, Montanuniversität Leoben, 8700 Leoben, Austria; nikolaus.preisser@unileoben.ac.at (N.P.); susanne.michelic@unileoben.ac.at (S.K.M.)
* Correspondence: shashank.ramesh-babu@unileoben.ac.at

Abstract: In situ study of the inclusion dissolution behavior in a slag utilizing high-temperature confocal scanning laser microscopy helps to understand the phenomenon of the removal of non-metallic inclusions from liquid steel before the casting process. The current work introduces an image processing procedure to automate and measure the inclusion diameter during its dissolution. Silica and alumina particle dissolution were considered as they appear differently when suspended in the slag (bubble-like transparent and solid-like opaque, respectively). The procedure consists of two parts: (1) morphological isolation and construction of the inclusion, and (2) inclusion diameter calculation. The inclusion diameters could be successfully measured over a series of images and showed good agreement with the manually measured diameters. The image processing procedure has the advantages of significant time saving and standardization compared to manual measurements.

Keywords: non-metallic inclusions; slag; image processing; MATLAB; confocal microscope; in situ; steel cleanliness

check for updates

Citation: Ramesh Babu, S.; Preisser, N.; Michelic, S.K. Image Processing Procedure to Evaluate Inclusion Dissolution in a Slag Observed by High-Temperature Confocal Scanning Laser Microscopy. *Metals* **2022**, *12*, 531. https://doi.org/10.3390/met12040531

Academic Editor: Lauri Holappa

Received: 19 February 2022
Accepted: 19 March 2022
Published: 22 March 2022

Publisher's Note: MDPI stays neutral with regard to jurisdictional claims in published maps and institutional affiliations.

Copyright: © 2022 by the authors. Licensee MDPI, Basel, Switzerland. This article is an open access article distributed under the terms and conditions of the Creative Commons Attribution (CC BY) license (https://creativecommons.org/licenses/by/4.0/).

1. Introduction

Steel cleanliness is decisive in the final product quality. In this context, effective removal of non-metallic inclusions (NMI) from the liquid steel before casting is essential. The aim is to transport inclusions to the steel/slag interface to ensure their separation into the slag and their final dissolution in the slag phase to avoid a possible re-entrapment in the steel. Slag properties and inclusion composition significantly influence the dissolution process. One possibility of studying the inclusion behavior in the steel–slag-refractory system in situ is high-temperature confocal scanning laser microscopy (HT-CSLM) [1]. This method was first introduced for metallurgical phenomena by Chikama et al. [2] in 1997. Since then, HT-CSLM has been applied to study different phase transformations [3–7] and for various inclusion related topics such as inclusion agglomeration in the liquid steel [8–10], reactions between inclusions and refractory material [11–13] as well as to observe inclusions acting as heterogeneous nuclei for a distinct microstructure formation [14]. Moreover, in situ studies on the dissolution behavior of different inclusion types essentially contributed to a deepened understanding of the dissolution process, its mechanisms, and the related influencing parameters [15–21]. Most research has been conducted on the dissolution behavior of oxide particles, mainly considering Al_2O_3, SiO_2, MgO, $MgAl_2O_4$, and $xCaOyAl_2O_3$ in the slag system $CaO–Al_2O_3–MgO–SiO_2$.

The experimental setup and procedure are well understood and optimized today. HT-CSLM is a state-of-the-art method to study the dissolution behavior of particles in a specific slag. However, the experimental data evaluation process is very time-consuming as it involves manual analysis and measurement of the particle diameter from individual frames in a video feed. Therefore, there is a need to introduce a standardized and time-efficient method to analyze the images.

Digital image processing involves extracting attributes and recognizing particular objects from an image [22]. Computer vision analysis techniques can help in producing repeatable and accurate results [23]. Image analysis has been shown to find applications in the analysis of phases in sintered steel and particle distribution in nickel super-alloys [24], porosity study in powder metallurgical alloys [25], evaluation of carbide coarsening [26], and analysis of carbides formed during the auto-tempering process in low-alloy martensitic steels [27].

The current work aims to introduce an image processing procedure to analyze inclusions during their dissolution in a slag under the HT-CSLM. A custom program was built using the Image Processing Toolbox in MATLAB (version 2021b, MathWorks, Inc., Natick, MA, USA) to run the analysis. Depending on the chemical compositions, inclusions such as alumina (Al_2O_3) can have an opaque appearance and silica (SiO_2) can have a bubble-like appearance when suspended in the slag. Therefore, two procedures were introduced to encompass both types of inclusions. The inclusion diameters measured during their dissolution in the slag with the image processing procedure were then compared to manually calculated results.

2. Materials and Methods

2.1. The Dissolution Experiment by Means of HT-CSLM

The general experimental setup at the Chair of Ferrous Metallurgy, Montanunivers itaet Leoben as well as the possibilities and limitations of HT-CSLM (laser microscope type VL2000DX, Lasertec, Yokohama, Japan and a high temperature furnace type SVF17-SP, Yonekura, Osaka, Japan) have already been described in detail in previous work [21]. An operating temperature of 1600 °C is usually chosen to simulate steelmaking temperatures. The gold-coated furnace chamber is flushed with argon to avoid the oxidation of the system during the dissolution process. For the experiments, a slag out of the system $CaO–Al_2O_3–SiO_2$ was used. The detailed slag composition is given in Table 1.

Table 1. Slag composition (wt %).

CaO	SiO_2	Al_2O_3	Na_2O
45.90	43.50	6.80	2.49

The performed steps for the dissolution experiments are as follows:

(1) The slag was prepared by mixing the raw materials and melting it in a top-loading laboratory furnace (Gero HTRV, Carbolite Gero, Sheffield, UK) at 1600 °C. A small amount of this slag was then ground and filled into a Pt-crucible, as seen in Figure 1.
(2) The slag was then pre-melted in the heating chamber of the HT-CSLM. This was to remove any air bubbles that might be trapped in the slag before conducting the experiment.
(3) A synthetic particle was placed on top of the slag. In this case, alumina and silica particles (Sandoz precision spheres, Cugy, Switzerland) with a diameter of 500 µm were chosen.
(4) The samples were subsequently heated to the experimental temperature of 1600 °C, and the dissolution of the inclusion was recorded throughout the whole experiment. A video of the dissolution process was stored. The sample was heated at a rate of 1000 °C/min to a temperature of 1400 °C to avoid any reaction between the inclusion and the slag. The heating was then gradually brought to an experimental temperature of 1600 °C. It should be noted that the silica inclusion started to dissolve in the melt already before reaching the experimental temperature. The alumina particle started to dissolve significantly in the slag only after reaching the experimental temperature. The microscope operator must choose and reassess the settings for contrast and brightness as well as the positioning in real-time to gain the best possible video data for further analysis.

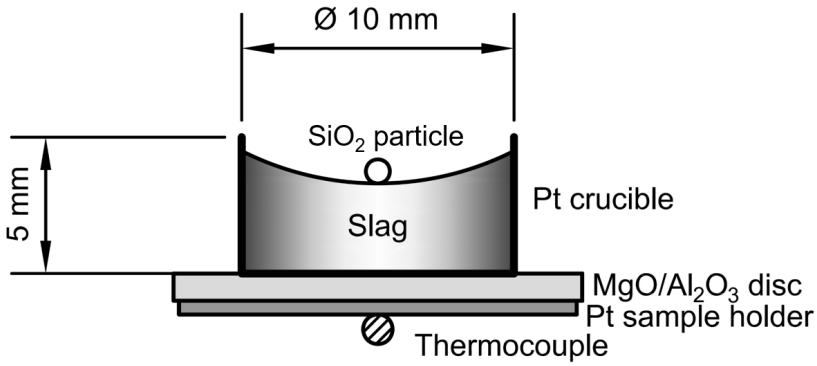


Figure 1. Schematic experimental setup of the dissolution of a synthetic SiO_2 'particle in the experimental slag by means of HT-CSLM, reproduced from [18], with permission from John Wiley and Sons, 2013. © 2013 The American Ceramic Society.

2.2. Evaluation of Dissolution Data

The manual measurement and calculation of the equivalent circle diameter (ECD) of the inclusion dissolution analysis of dissolution behavior was conducted as follows:

(1) A suitable timeframe of dissolution of the particle was chosen from the video. Time zero of the experiment was set when the experimental temperature of 1600 °C was reached. In the case of the silica particles, the time zero was whenever it started to significantly dissolve in the slag. This was at around 1550 °C in the current study.
(2) The video data sequence from time zero until complete particle dissolution was selected using the software VirtualDub (version v1.10.4, Avery Lee) [28].
(3) The same software was used to convert the video into a series of images. This was approximately a hundred images.
(4) A set of images of the dissolution of SiO_2 in the experimental slag composition can be seen in Figure 2. These images represent (a) time zero, (b) 20 s of dissolution, (c) 40 s of dissolution, and (d) 60 s of dissolution.

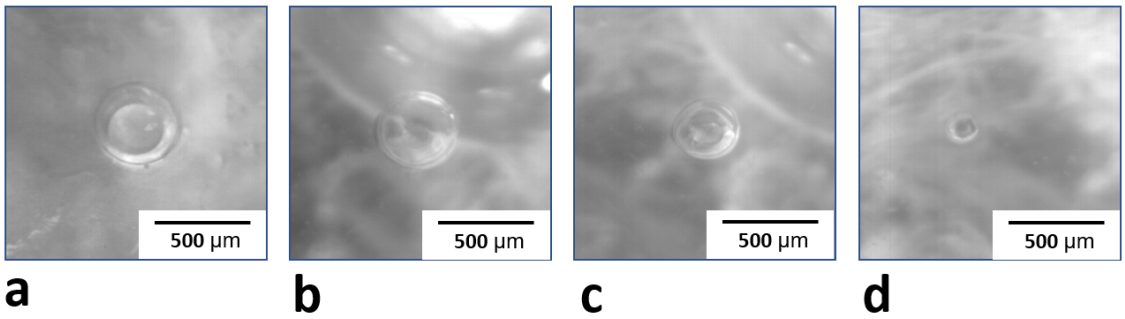


Figure 2. Dissolution of the synthetic silica ,particles in the experimental slag where the images were taken at, (**a**) time zero, (**b**) 20 s of dissolution, (**c**) 40 s of dissolution, and (**d**) 60 s of dissolution.

After the extraction of a sufficient number of frames, the images can be analyzed with the software "Jens Rüdigs Makroaufmaßprogramm" [29]. This analysis consists of the following steps:

(1) Definition of the scale of the images.
(2) Tracing of the perimeter of the particles by computer mouse aim. The software then provides the area of the traced particles.
(3) Conversion of the measured area to ECD for comparison.

2.3. Data Evaluation Using Image Processing

The Image Processing Toolbox on MATLAB was used to design the inclusion dissolution diameter calculation program. The program can be divided into two parts. The

first part concerns the morphological construction of the inclusion. The second part is the calculation of the diameter of the constructed inclusion. The morphology construction part of the program, if the inclusion has a translucent bubble-like appearance, roughly consists of the following steps:

(1) The video output obtained from the HT-CSLM microscope was first sequenced into a series of images using the VirtualDub (version v1.10.4, Avery Lee) software. A representation of the grey-scale image of the bubble-like inclusion can be seen in Figure 3a.
(2) The edge detection command was used to identify all the discontinuities of the object in the image. The Canny method [30] was found to be the best for detecting edges of the inclusions from the images under consideration in this work. The schematic of the output after the edge detection was in a binary image form, as shown in Figure 3b.
(3) The image was then transformed into a solid particle by the morphological methods of dilatation of the edges and further filled up any perforations that may occur within the regions with white pixels. This procedure can cause oversizing of the region, which represents the inclusion as seen in Figure 3c.
(4) The image was then subjected to erosion wherein the outer edges were cleaned to roughly obtain the same shape, as seen in the grey-scale image. The results can be seen in Figure 3d.

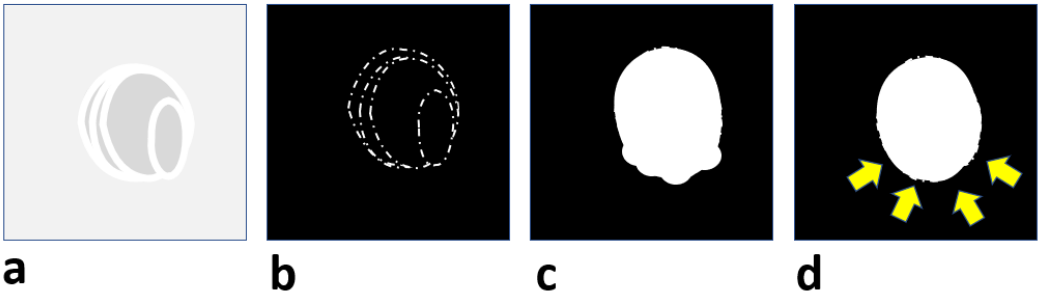


Figure 3. Schematic of the morphological construction of a bubble-type inclusion from the greyscale imagewhere, (**a**) represents the bubble-like inclusion, (**b**) the inclusion after the edges are detected, (**c**) inclusion further transformed into a solid particle and, (**d**) the cleaned and corrected inclusion morphology.

The morphology construction part of the program, if the inclusion has an opaque solid-type appearance, roughly consists of the following steps:

(1) As described in the earlier paragraph, the video output was first sequenced into a series of images using the VirtualDub (version v1.10.4, Avery Lee) software. A representation of the grey-scale image of the solid-type inclusion can be seen in Figure 4a. Artifacts represented with a lighter shade of gray compared to the inclusion can also be seen in the figure.
(2) The Canny edge detection command was used to identify all the discontinuities of the objects in the image. The schematic of the output after the edge detection was in a binary image, as shown in Figure 4b.
(3) All the edges were first dilated. Then, the image was complemented so that all the black pixels became white and vice versa. The resulting image can be seen in Figure 4c.
(4) All of the regions connected to the edges of the picture were removed. The image with the inclusion and any remaining artifacts can be seen in Figure 4d.

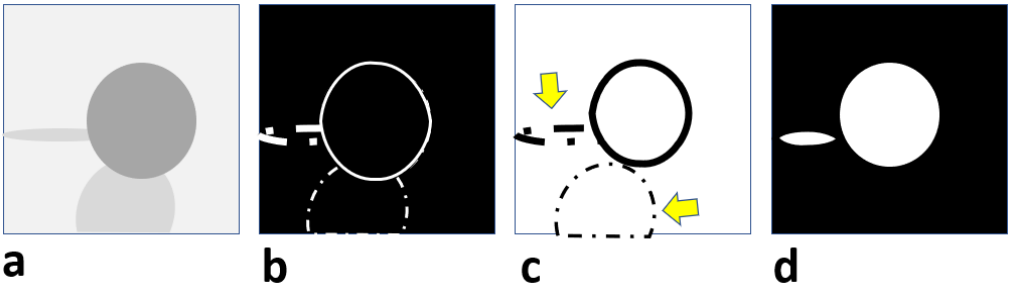


Figure 4. Schematic of the morphological construction of a solid-type inclusion from the greyscale image where, (**a**) represents the solid-like inclusion, (**b**) the inclusion after edges detected, (**c**), the image was complimented and, (**d**), the inclusion morphology retained after removal of major artifacts.

The second part of the program involves the determination of the equivalent circle diameter (ECD) of the shape representing the inclusion [31]. The steps to process them are as follows:

(1) The perimeters and areas of all the morphologically constructed regions, as seen in Figure 5a, are calculated. Then, the value of circularity is indexed to all regions. The used formula is given in Equation (1).

$$Circularity = \frac{(Perimeter)^2}{4 \times \pi \times Area} \quad (1)$$

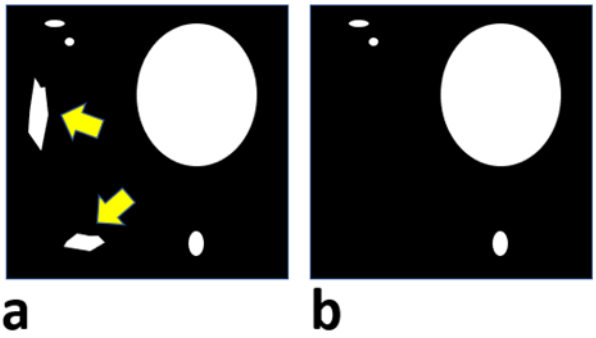


Figure 5. Schematic that shows elimination of the irregular shaped regions by using circularity as a threshold where, the irregular shaped artifacts as seen in (**a**) (indicated by arrows) are removed which results in the inclusion with only minor artifacts as seen in (**b**).

(2) The regions that are indexed outside of a circularity range (considering that a value of 1 represents a perfect circular shape as per the calculation in Equation (1), a parameter range of circularity was chosen so that all circular and near circular objects were selected) are discriminated, thereby leaving behind an image of mostly circular shapes. This is represented by the schematic shown in Figure 5b.
(3) The diameters of the remaining regions within the processed image are then determined. Only the diameters of the largest regions are then output as the final diameter of the inclusion.

3. Results

An example of the image processing tool in operation can be seen in Figure 6. The HT-CSLM microscopy image of the silica inclusion suspended in the slag can be observed in Figure 6a. Unlike the schematic as seen in Figure 3, the image in Figure 6 has small air bubbles suspended in the slag. Scratches and the other imperfections on the bottom of the crucible can also be found. The next step was to use the edge detection module on the Image Processing Toolbox. The Canny algorithm was found to be the most suitable for the current images. The output after implementing the detection can be seen in Figure 6b. The

white pixel regions were then dilated, as shown in Figure 6c. This was to ensure that the region representing the inclusion becomes a solid. Any perforations within the regions were then filled up using the hole filling MATLAB image processing operation. Finally, all the regions smaller than 1000 pixels were removed and an erosion command was used to remove any projections around the inclusion. The resulting image after the completion of the morphological operations can be seen in Figure 6d.

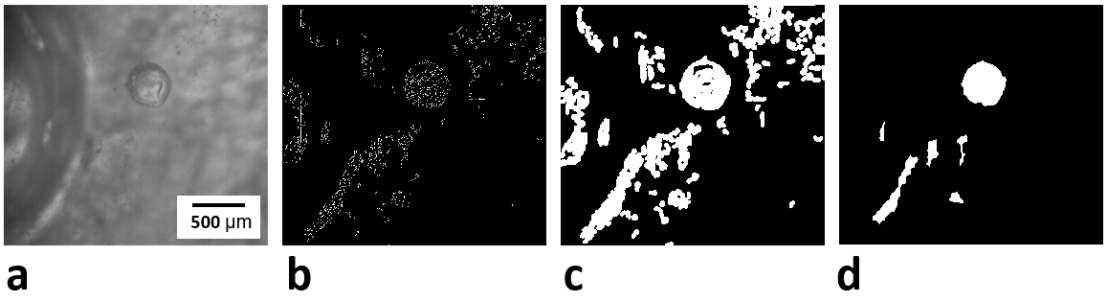


Figure 6. (**a**) HT-CSLM microscopy image of the silica inclusion suspended in the slag at a temperature of 1550.4 °C and time 467.81 s. (**b**) Image of the inclusion after running the Canny edge detection method on Figure 3a. (**c**) Dilated image of the inclusion, which was segmented by edge detection. (**d**) Morphologically constructed inclusion after a sequence of erosion and hole-filling operation on MATLAB.

The HT-CSLM micrograph of the alumina inclusion suspended in the slag can be found in Figure 7a. As seen in the schematic shown in Figure 4b, the image was subjected to the Canny edge detection procedure, resulting in Figure 7b. The edges were first dilated and then complemented to convert the black regions into white and vice versa. The resultant image is the inclusion represented by the white almost circular region and the artifact regions, as given in Figure 7c. The white regions connected to the edge of the images and the remaining artifacts similar to the ones described in the previous were removed, resulting in an image with only the alumina inclusion. This is represented by the white circle-like region, as illustrated in Figure 7d.

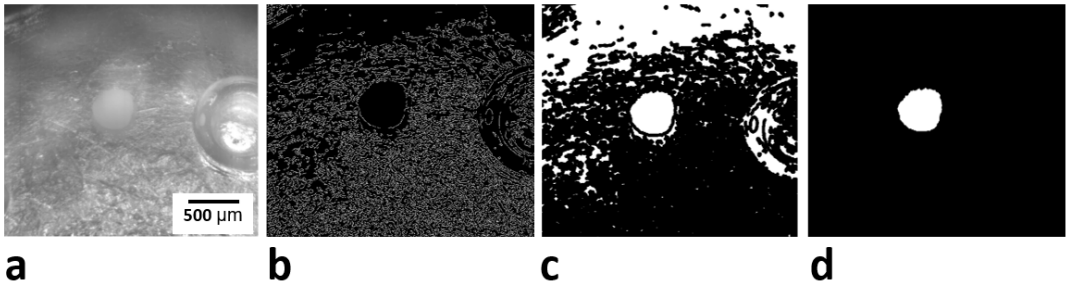


Figure 7. (**a**) HT-CSLM microscopy image of the alumina inclusion suspended in the slag at a temperature of 1600 °C and time 525.15 s. (**b**) Image of the inclusion after running the Canny edge detection method on Figure 4a. (**c**) Image after the dilation of edges in Figure 4b and binary color complement procedure. (**d**) Morphologically constructed inclusion after removing regions connected to boundaries of the picture and the regions outside the circularity threshold.

The areas and perimeters of all the regions in Figures 6d and 7d were determined and the circularity was calculated. The most irregularly shaped regions were removed using the circularity threshold value ranging between 0.8 to 3 for silica and 0.8 to 10 for alumina. The centroids, major, and minor axis to these centroids of the white pixel regions in the image were then calculated. The mean of the major and minor axis to the centroids resulted in diameters. The red circles constructed using these diameters can be seen in Figure 8.

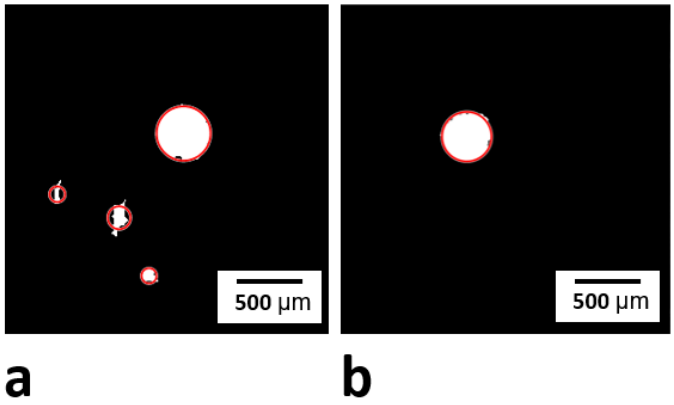


Figure 8. Image of the morphologically processed (**a**) silica and (**b**) alumina inclusion with the red circle drawn from the diameter calculated as described by the steps in the Section 2.

The diameters of the inclusions in the image sequence were then measured and are represented by the red circles as in the scatterplot in Figure 9. These were compared with the manually calculated diameters of the inclusions, which are indicated by blue and green triangles corresponding to the silica and alumina, respectively. The scatter plot suggests that both the results are a good fit.

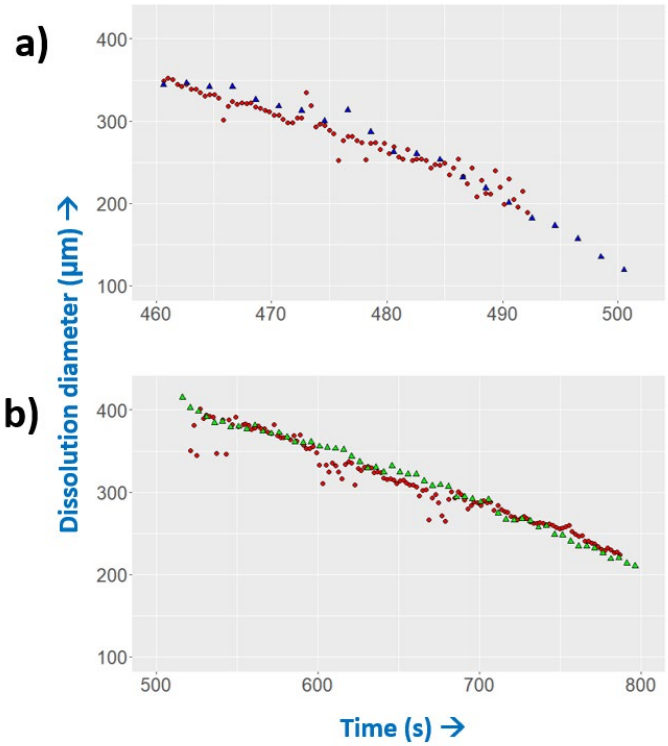


Figure 9. Plot showing the diameters of the (**a**) silica and (**b**) alumina inclusions during its dissolution in the slag. The red circles are the diameters as calculated by the image processing program. The blue and green triangles represent the manually measured diameters of the silica and alumina inclusion, respectively.

4. Discussion

The manual measurement of the inclusion diameter from the image sequence data is time consuming, as it includes tracing the particles using the mouse aim and noting the measured area and the time and temperature of the respective image frame. Manual measurement by an experienced user would take approximately a little over a minute per image. Therefore, manually measuring 100 images from each experiment would take

about 1.5–2 h. Additionally, there is a degree of variability depending on the individual who measures the inclusion diameter. This is due to the blurry borders of the particles, shadows, and scratches on the bottom of the crucible combined with the manual tracing of the inclusion with the computer mouse aim. Therefore, it is advantageous to utilize an automated measurement of the diameters from the images.

A transparent slag is a pre-condition for good observation conditions in the experiment itself as well as for subsequent data evaluation. This has been observed for many compositions in the classical system $CaO–SiO_2–Al_2O_3–MgO$ [15–21] and is also valid for the investigated slag composition in the present study. Additions of FeO, MnO, and TiOx are reported to have a negative influence on slag transparency.

The quality of the HT-CSLM microscopy images is a major limiting factor in designing a convenient image processing tool for automating the diameter measurement during inclusion dissolution. In an ideal scenario, the image would have high contrast and sharpness [32], which would help distinguish the inclusion from its surroundings. This would then allow for an easy image processing operation. However, inclusions, as captured using the HT-CSLM microscopy, were not very discernible. This is because of the regular focus and contrast control adjustments of the lens, which is unavoidable by the operator. Artifacts such as air bubbles, scratches, and other imperfections found on the bottom of the crucible further decreases the quality of the image. Any flat part of the bottom of the crucible reflects the laser, thereby causing regions of bright areas. In addition, there is a low contrast between the inclusion and the slag in which it is suspended. This makes the inclusion shape detection a significant challenge. This is very evident in Figure 10 wherein a simple binary image conversion with an automatic thresholding of Figures 6a and 7a results in a poor image. It could be possible to slightly improve the inclusion's contrast and sharpness when the images are inspected individually. However, this cannot be automated into an image processing program for diameter measurements. The edge detected image as seen in Figures 6b and 7b is therefore the most convenient method to detect the inclusions from the microscopy images.

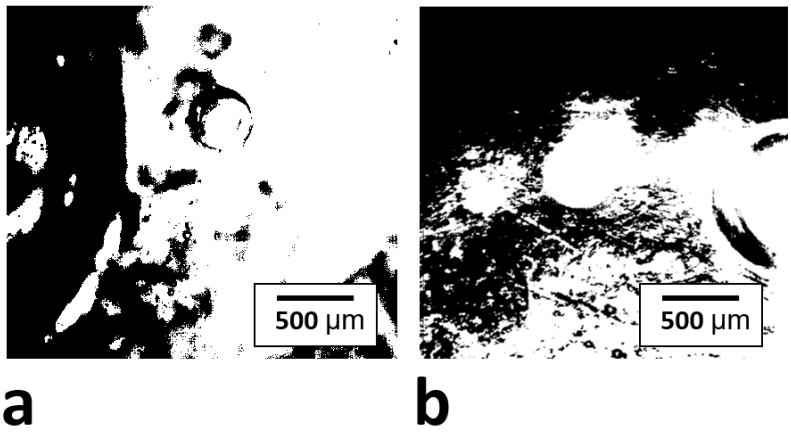


Figure 10. Binarized black and white image of the HT-CSLM microscopy image of (**a**) the silica particle as seen in Figure 6a and (**b**) alumina particles as seen in Figure 7a.

Edge detection algorithms work by detecting the discontinuities of objects within the image [33]. There are various detection methods found in MATLAB such as the Sobel and Prewitt. The Canny edge detection algorithm [30] in the MATLAB Image Processing Toolbox was found to be the best suited. The general methodology of the Canny is that it finds edges by looking for the local maxima of the gradients in the image edges [34]. It uses a two-threshold method to detect strong and weak edges. Other approaches found within the edge detection tool in MATLAB were unable to detect most of the edges of the inclusions. Due to the two threshold calculations, the Canny method is less likely to be influenced by noise, and therefore more likely to detect weak edges [34].

The morphological construction of the inclusion from the HT-CSLM microscopy images is the logical first step before its dimensions can be measured in an automated manner. The solid and the bubble-like appearances of the alumina and silica, respectively, when suspended in the molten slag require different morphological construction procedures as documented in the Materials and Methods section. After the construction of white regions representing the inclusion against a black background, the diameter measurement procedural steps for both types of inclusions are the same.

The detection of circularity is a challenge as there can be image artifacts that are originally not part of the inclusion that can merge into it during the morphological construction operation. This is evident in Figure 11a, wherein the artifacts around the silica inclusion are detected during the edge detection operation as seen in Figure 11b. These artifacts become much larger and are included as part of the inclusion during the pixel dilation operation, as seen in Figure 11c. The protrusion artifact is not eliminated during the erosion operation as seen in Figure 11d. Any further modifications to the code cause errors during the measurement of inclusion diameters in the other images. These inclusions with protrusions would therefore not be detected if the circularity value of 1 is used as a threshold value (which represents a perfect circle). It is for this reason that an appropriate range of circularities (0.8 to 3 for silica and 0.8 to 10 for alumina in this study) was used as a threshold to ensure that all possible circular or near circular shaped regions were considered for the diameter calculation. In other words, the threshold range is dependent on the variability of the quality and the artifacts found in the image sequences. Therefore, the circularity range can be considered as an adjustable parameter for each image sequence analyzed.

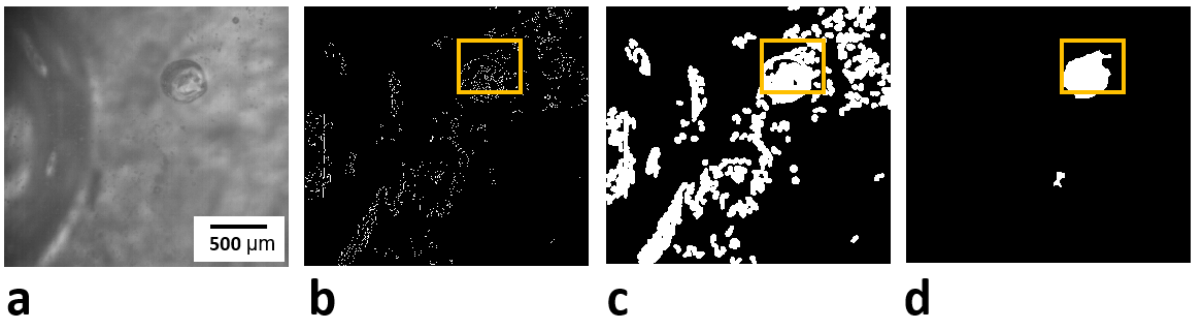


Figure 11. (**a**) HT-CSLM microscopy image of the silica inclusion suspended in the slag at a temperature of 1558.8 °C and time 473.40 s. (**b**) Image of the inclusion after running the Canny edge detection method on Figure 3a. (**c**) Dilated image of the inclusion that was segmented by edge detection. (**d**) Morphologically constructed inclusion after a sequence of erosion and hole-filling operation on MATLAB.

Blurriness is another reason for causing incorrect inclusion diameter measurements in some images. Two examples can be seen in Figure 12. The blur is caused by the fast motion of the inclusion in the slag. This is even more pronounced when the inclusions are smaller in size and are moving much faster when compared to the larger inclusions in the slag at higher temperatures. The blurriness of the inclusions therefore leads to noise and outliers in the inclusion diameter scatterplot, as seen in Figure 9. The noise in the plot for smaller diameters is due to the increasing interference from the artifacts in the image background, which are then of a comparable size of the inclusions and the blurriness caused by the increased speed in motion of the inclusion in the slag. This leads to overestimation of the diameter.

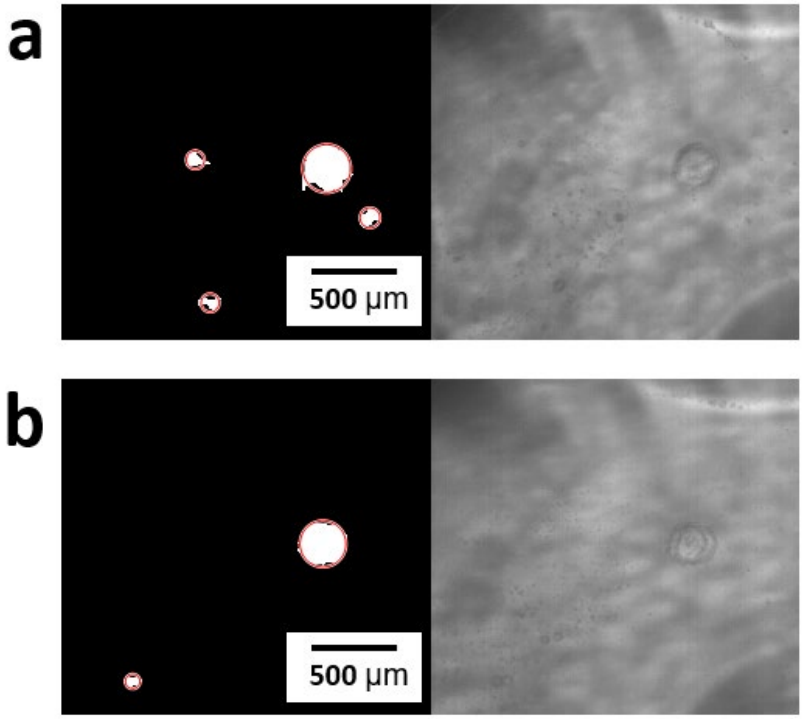


Figure 12. Images showing the morphologically constructed inclusion and the corresponding HTSC microscopy images showing a blurry silica inclusion recorded at (**a**) 1577.7 °C and at time 486.17 s and (**b**) 1579.6 °C and at time 487.36 s.

The plots as seen in Figure 9 show that there was only a minor difference between the diameters calculated by the image processing program and the manual calculations. The program took about 30 s to process the image sequence instead of a few hours when conducted by the manual method. There was also a degree of inconsistency during the manual determination of the diameter. The automated way of diameter measurement can mitigate this by employing image processing.

The tool requires that the image sequence should be of consistent image quality. Otherwise, there can be significant errors in the detection of the inclusion diameters. Another issue is that the code requires some adjustments such as the circularity threshold, which depends on the quality of the image sequence. However, the basic procedure of constructing the morphology of both the bubble-type and solid-type inclusion and then the subsequent measurement of the diameter as stated in this work still holds. The time saved to make the image series measurements and determine the dissolution trend is significant. This validates the usage of an image processing procedure to calculate the diameters of the inclusions during its dissolution in the slag under the HT-CSLM microscope.

5. Conclusions

The paper successfully demonstrates an image processing procedure to automate the diameter measurement of inclusions during their dissolution in a slag under a HT-CSLM microscope. The dissolution of an alumina and a silica particle were considered as they have a solid-like opaque and bubble-like translucent appearance, respectively, when suspended in the slag. A video of the inclusion dissolution in the slag was captured and then sequenced into a series of images. The image processing program consisted of two parts: morphological construction of the inclusion shape and the inclusion diameter measurement. In the morphological construction part, the inclusion was isolated from the image's background. The procedure differed depending on the appearance of the inclusion suspended in the slag, namely, bubble and solid-like appearance. After isolating the inclusion morphology and artifacts, the circularity of all regions was calculated. A circularity threshold was calculated so that only the inclusion was considered. The diameter

of the inclusion was then calculated. Running this procedure over a series of images resulted in a considerable saving of time compared to manually measuring the inclusion diameter. The comparison of the results between the image processed and manually measured diameters were satisfactory. The aim in the future would be to couple the image processing program with another tool that can evaluate the dissolution mechanism. This program would then provide significant scientific output, specifically, the dissolution mechanisms and the related diffusion coefficients from various experiments as previously described by Feichtinger et al. [18] and Michelic et al. [21] in a short time.

Author Contributions: Conceptualization, S.R.B.; Methodology, S.R.B. and N.P.; Software, S.R.B.; Validation, S.R.B. and S.K.M.; Formal analysis, S.R.B.; Investigation, S.R.B.; Resources, N.P.; Data curation, S.R.B. and S.K.M.; Writing—original draft preparation, S.R.B., N.P. and S.K.M.; Writing—review and editing, S.R.B. and S.K.M.; Visualization, S.R.B.; Supervision, S.K.M.; Project administration, S.K.M.; Funding acquisition, S.K.M. All authors have read and agreed to the published version of the manuscript.

Funding: The financial support by the Austrian Federal Ministry for Digital and Economic Affairs, the National Foundation for Research, Technology and Development, and the Christian Doppler Research Association is gratefully acknowledged.

Data Availability Statement: Not applicated.

Conflicts of Interest: The authors declare no conflict of interest.

References

1. Sridhar, S. Application of Confocal Scanning Laser Microscopy to Steel Research. In Proceedings of the ICS 2005-3rd International Congress on the Science and Technology of Steelmaking, Charlotte, NC, USA, 9–12 May 2005; pp. 797–810.
2. Chikama, H.; Shibata, H.; Emi, T.; Suzuki, M. In-situ real time observation of planar to cellular and cellular to dendritic transition of crystals growing in Fe-C alloy metls. *Mater. Trans. JIM* **1196**, *37*, 620–626. [CrossRef]
3. Phelan, D.; Reid, M.H.; Dippenaar, R. High Temperature Laser Scanning Confocal Microscopy for Real-time Studies of Phase Transformations. *Microsc. Microanal.* **2005**, *11*, 670–671. [CrossRef]
4. Reid, M.; Phelan, D.; Dippenaar, R. Concentric Solidification for High Temperature Laser Scanning Confocal Microscopy. *ISIJ Int.* **2004**, *44*, 565–572. [CrossRef]
5. Liang, G.F.; Wan, C.Q.; Wu, J.C.; Zhu, G.M.; Yu, Y.; Fang, Y. In situ observation of growth behavior and morphology of delta-ferrite as function of solidification rate in an AISI304 Stainless Steel. *Acta Metall. Sin.* **2006**, *19*, 441–448. [CrossRef]
6. Liu, Z.; Kobayashi, Y.; Yang, J.; Nagai, K.; Kuwabara, M. In-situ observation of the delta/gamma phase transformation on the surface of low carbon steel containing phosphorus at various cooling rates. *ISIJ Int.* **2006**, *46*, 847–853. [CrossRef]
7. Nassar, H.; Fredriksson, H. On peritectic reactions and transformations in low-alloy steels. Metallurgical and Materials Transactions A. *Metall. Mater. Trans. A* **2010**, *41*, 2776–2783. [CrossRef]
8. Yin, H.; Shibate, H.; Emi, T.; Suzuki, M. Characteristics of agglomeration of various inclusion particles on molten steel surface. *ISIJ Int.* **1997**, *37*, 946–955. [CrossRef]
9. Yin, H.; Shibate, H.; Emi, T.; Suzuki, M. In-situ observation of collision, agglomeration and cluster formation of alumina inclusion particles on steel melts. *ISIJ Int.* **1997**, *37*, 936–945. [CrossRef]
10. Mu, W.; Dogan, N.; Coley, K.S. Agglomeration of non-metallic inclusions at steel/ar interface: In-situ observation experiments and model validation. *Metall. Mater. Trans. B* **2017**, *48*, 2379–2388. [CrossRef]
11. Salgado, U.D. Investigation of Particle Attraction by Steel/Refractory and Steel/Gas Interfaces. Ph.D. Thesis, Montanuniversität Leoben, Leoben, Austria, 2018.
12. Michelic, S.K.; Diéguez-Salgado, U.; Bernhard, C. In-situ observation of the behaviour of non-metallic inclusions at different interfaces in the system steel-slag-refractory. *IOP Conf. Ser. Mater. Sci. Eng.* **2016**, *143*, 012010. [CrossRef]
13. Misra, P.; Chevrier, V.; Sridhar, S.; Cramb, A.W. In situ observations of inclusions at the (Mn, Si)-killed steel/CaO-Al_2O_3 interface. *Metall. Mater. Trans. B* **2000**, *31*, 1135. [CrossRef]
14. Loder, D.; Michelic, S.K.; Mayerhofer, A.; Bernhard, C. On the capability of nonmetallic inclusions to act as nuclei for acicular ferrite in different steel grades. *Metall. Mater. Trans. B* **2017**, *48*, 1992–2006. [CrossRef]
15. Miao, K.; Haas, A.; Sharma, M.; Mu, W.; Dogan, N. In situ observation of calcium aluminate inclusions dissolution into steelmaking slag. *Metall. Mater. Trans. B* **2018**, *49*, 1612–1623. [CrossRef]
16. Fox, A.B.; Valdez, M.; Gisby, J.; Atwood, R.C.; Lee, P.D.; Sridhar, S. Dissolution of ZrO_2, Al_2O_3, MgO and $MgAl_2O_4$ particles in a B_2O_3 containing commercial fluoride-free mould slag. *ISIJ Int.* **2004**, *44*, 836–845. [CrossRef]
17. Monaghan, B.J.; Chen, L. Dissolution behavior of alumina micro-particles in CaO-SiO_2-Al_2O_3 liquid oxide. *J. Non-Cryst. Solids* **2004**, *347*, 254–261. [CrossRef]

18. Feichtinger, S.; Michelic, S.K.; Kang, Y.-B.; Bernhard, C. In-situ observation of the dissolution of SiO_2 particles in $CaO-Al_2O_3-SiO_2$ slags and mathematical analysis of its dissolution pattern. *J. Am. Ceram. Soc.* **2014**, *97*, 316–325. [CrossRef]
19. Monaghan, B.J.; Chen, L. Effect of changing slag composition on spinel inclusion dissolution. *Ironmak. Steelmak.* **2006**, *33*, 323–330. [CrossRef]
20. Vantilt, S.; Coletti, B.; Blanpain, B.; Fransaer, J.; Wollants, P.; Sridhar, S. Observation of inclusions in manganese-silicon killed steels at steel-gas and steel-slag interfaces. *ISIJ Int.* **2004**, *44*, 1–10. [CrossRef]
21. Michelic, S.K.; Goriupp, J.; Feichtinger, S.; Kang, Y.-B.; Bernhard, C.; Schenk, J. Study on oxide inclusion dissolution in secondary steelmaking slags using high temperature confocal scanning laser microscopy. *Steel Res. Int.* **2016**, *87*, 57–67. [CrossRef]
22. Gonzalez, R.C.; Woods, R.E. *Digital Image Processing*, 3rd ed.; Pearson/Prentice Hall: Upper Saddle River, NJ, USA, 2007; ISBN 013168728X.
23. Holm, E.A.; Cohn, R.; Gao, N.; Kitahara, A.R.; Matson, T.P.; Lei, B.; Yarasi, S.R. Overview: Computer vision and machine learning for microstructural characterization and analysis. *Metall. Mater. Trans. A* **2020**, *51*, 5985–5999. [CrossRef]
24. Komenda, J. Automatic recognition of complex microstructures using the Image Classifier. *Mater. Charact.* **2001**, *46*, 87–92. [CrossRef]
25. Marin, M.; Marin, F.B. Quantitative image analysis in some iron powder metallurgy materials. *IOP Conf. Ser. Mater. Sci. Eng.* **2019**, *485*, 12011. [CrossRef]
26. Mesquita, R.A.; Barbosa, C.A. Spray forming high speed steel—properties and processing. *Mater. Sci. Eng. A* **2004**, *383*, 87–95. [CrossRef]
27. Ramesh Babu, S.; Davis, T.P.; Haas, T.; Jarvenpää, A.; Kömi, J.; Porter, D. Image processing tool quantifying auto-tempered carbides in as-quenched low carbon martensitic steels. *Metals* **2020**, *10*, 171. [CrossRef]
28. Lee, A. Virtualdub. 1991.
29. Ruedig, J. Jens' Makroaufmass-Programm.
30. Canny, J. A Computational approach to edge detection. *IEEE Trans. Pattern Anal. Mach. Intell.* **1986**, *PAMI-8*, 679–698. [CrossRef]
31. Image Analyst. Which One is Best for Calculating Circularity? Available online: https://de.mathworks.com/matlabcentral/answers/85363-which-one-is-best-for-calculating-circularity (accessed on 19 November 2021).
32. Adams, F.; Barbante, C. Spatially confined analysis. In *Chemical Imaging Analysis*; Elsevier: Amsterdam, The Netherlands, 2015; pp. 29–66, ISBN 9780444634399.
33. Ziou, D.; Tabbone, S. Edge detection techniques: An overview. *Pattern Recognit. Image Anal. C/C Raspoznavaniye Obraz. I Anal. Izobr.* **1998**, *8*, 537–559.
34. MATLAB. Edge. Available online: https://de.mathworks.com/help/images/ref/edge.html (accessed on 19 November 2021).